Effects of Microstructural Evolution and Dislocation Properties on the Strengthening Behavior of Cold-Drawn Ultralow-Carbon Steel

AKIRA TANIYAMA, MASAHIRO ARAI, MAKOTO KOSAKA, and TAKANARI HAMADA

The microstructural evolution and variations in the dislocation properties and the dislocation density of drawn ultralow-carbon (ULC) steel wires, which exhibited an ultimate tensile strength of over 1500 MPa at $\varepsilon = 5.3$, were investigated through scanning electron microscopy/electron backscatter diffraction (SEM/EBSD) analysis and synchrotron radiation X-ray diffraction (SR-XRD), respectively. The wire drawing did not cause systematic changes in the dislocation properties of the drawn ULC steel wire. Dislocation strengthening and the grain size effect, such as the Bailey–Hirsch relationship and the Langford–Cohen relationship, were found to be dominant in the early and subsequent stages of drawing, respectively. Moreover, tensile strength of the drawn ultralow-carbon steel wires at $\varepsilon > \sim 4$ showed a positive deviation from the extrapolated Langford–Cohen relationship in the early stages of drawing, which was found to be caused by changes in the character of grain boundaries during drawing, that is, an increase in the fraction of grains surrounded by boundaries with misorientation angles of 15 deg or greater and a relative decrease in the fraction of low-angle boundaries with misorientation angles of less than 5 deg contributed to the excessive strengthening in the drawn ULC steel wires.

I. INTRODUCTION

WORK-HARDENING and structural refining are important technologies for strengthening metallic materials, such as steel products. Accumulative roll bonding (ARB),[1,2] equal-channel angular pressing (ECAP),[3–5] mechanical milling (MM),[6–8] and high-pressure torsion (HPT)[9–11] are established techniques for achieving severe plastic deformation and obtaining fine crystalline grains. Cold drawing is a particularly important technique in industrial production processes for fabricating steel wires with high tensile strength. In their pioneering research, Langford and Cohen investigated the work-hardening behavior of iron wires and found that the true tensile strength linearly increased with the inverse of the mean distance between transverse intercepts of grain boundary elongated in the direction parallel to the wire axis,[12] which is referred to as the Langford–Cohen relationship. Their experimental results were quantitatively compared by Kuhlmann–Wilsdorf using the work-hardening theory.[13] Recent studies conducted using cold-drawn pure iron wires with nano-lamellar structures concluded that the flow stress increased in a manner similar to the Langford–Cohen relationship.[14,15]

Even in drawn pearlitic steel wires, microstructural evolution has been found to influence the increase in tensile strength.[16–21] The strength of pearlitic steel wires is known to be inversely proportional to the square root of the lamellar spacing based on the Hall–Petch relationship.[22,23] Additionally, the partial dissolution of cementite (Fe_3C) has been suggested to occur in heavily cold-drawn pearlitic steel and significantly contribute to increasing the strength.[24–28] Recently, the maximum tensile strength of over 6 GPa was obtained for pearlitic steel with hypereutectoid composition by a severe cold-drawing process.[29]

The strength of ultrafine-grained metals has been found to exhibit a positive deviation from the extrapolated Hall–Petch relationship in coarse grains of

AKIRA TANIYAMA is with the Advanced Technology Research Laboratories, Nippon Steel Corporation, 1-8 Fuso-cho Amagasaki, Hyogo 660-0891, Japan. Contact e-mail: taniyama.76c.akira@jp.nipponsteel.com MASAHIRO ARAI is with the Nippon Steel Research Institute Corporation, 1-8 Fuso-cho, Amagasaki, Hyogo 660-0891, Japan. MAKOTO KOSAKA is with the Steel Research Laboratories, Nippon Steel Corporation, 20-1 Shintomi, Futtsu, Chiba 293-8511, Japan. TAKANARI HAMADA is with the Nagoya Marketing Branch, Nippon Steel Corporation, 13-18, Meiekiminami 2-chome, Nakamura-ku, Nagoya, Aichi 450-0003, Japan.

ultralow-carbon interstitial-free (IF) steel.[30,31] Similar phenomena have also been observed in pure aluminum[32–34] and pure copper.[35] This behavior, which is termed as "extra Hall–Petch strengthening," is believed to be induced by the extremely high stress required by the ultrafine-grained samples to yield, owing to the lack of dislocation sources in the grain. Furthermore, dislocations in the low-angle boundaries in sub-grained samples act as active dislocation sources, leading to lower yield stresses.[36] The extra Hall–Petch strengthening, which has been primarily observed in the ultrafine grains produced by ARB and plasma sintering, has rarely been reported in the grains produced by cold drawing. Because the ferrite phase (bcc-Fe) carries most of the strain in pearlitic steel wires during the process of drawing, the potential of excessive strengthening similar to the extra Hall–Petch strengthening in the ferrite phase of the drawn pearlitic steel may contribute significantly to increasing the strength and partial dissolution of cementite.

In this study, the internal structural changes of ultralow-carbon steel wires drawn by the cold-drawing method, which have a considerably simpler microstructure consisting only of the ferrite phase compared to that of pearlitic steel wires, were investigated by conducting microstructural examination (scanning electron microscopy; SEM) and dislocation analysis (synchrotron radiation X-ray diffraction; SR-XRD). Based on microstructural characteristics such as grain size, grain boundary properties, dislocation properties such as the fraction of screw and edge dislocation components and the dislocation arrangement, and dislocation density, the hardening behavior and microstructural evolution of the drawn ultralow-carbon steel wires were experimentally clarified to confirm the possible occurrence of excessive strengthening similar to the extra Hall–Petch strengthening, and the factors responsible for the strengthening were investigated.

II. MATERIALS AND METHODS

A. Materials

A billet of ultralow-carbon (ULC) steel was prepared by laboratory melting. The chemical composition of the ULC steel is listed in Table I. An initial steel wire was produced by drawing the ULC steel billet. To suppress grain coarsening during recrystallization, this wire was heated at 1210 K for 7 seconds, cooled to 916 K at 18.375 K/s, maintained at 916 K for 12 seconds, and cooled gradually thereafter. Subsequently, the heat-treated initial steel wire with a diameter of 3.245 mm was drawn using four steps of dry drawing from 3.245 to 1.972 mm, followed by 26 steps of wet drawing from 1.972 to 0.198 mm. Tensile tests were performed at a constant speed of 5 mm/min.

B. Internal Structure Analysis by SEM

A longitudinal cross-section of the drawn steel wire along the direction of drawing was used as a sample for the internal structure analysis as shown in Figure 1(a).

Table I. Chemical Composition of the Ultralow-Carbon Steel Sample (Mass Pct)

C	Si	Mn	P	S	Cr	N
0.003	0.2	0.5	0.011	0.001	0.08	0.0018

The sample surfaces were mechanically polished using abrasive paper, diamond-based slurry, and the chemical–mechanical polishing technique using a colloidal silica-based slurry. Internal structure observations with electron channeling contrast (ECC) and electron backscatter diffraction (EBSD) experiments were performed at 20 kV using a field-emission SEM apparatus (Carl Zeiss Ultra55) and an EBSD detector camera (EDAX DigiView) to determine the orientation and shape of the internal structure. The EBSD data were analyzed using the OIM Analysis software provided by EDAX.

C. Synchrotron Radiation X-Ray Diffraction Experiments

Thin plate samples with a longitudinal cross-section along the wire drawing direction were used for the SR-XRD analysis. The plate samples were prepared by mechanical grinding and polishing. The plate thickness was adjusted to 0.2 mm considering the penetration length of the X-rays used in this study. The SR-XRD experiments were performed at the Engineering Science Research beamline (BL19B2) at SPring-8 (Japan) using collimated monochromatic X-rays with a slit measuring 0.3 mm (V) × 3 mm (H). A schematic of this experiment is shown in Figure 1(b). The monochromatic X-ray wavelength was calibrated to 0.049944 nm using the standard diffraction profile of silicon powder. The transmitted and diffracted X-rays were recorded using an imaging plate (IP; Fujifilm, BAS-MS2040: 50 μm/pixel) mounted on a Debye–Scherrer camera with a radius of 286.5 mm. The diffraction profiles were captured after setting the exposure time to 60 seconds. During the exposure, the sample was swiveled from − 3 to 3 deg to investigate the contribution of the increased number of crystalline grains to the diffraction profile. The diffraction profiles recorded after the exposure were scrutinized using an IP reader (Fujifilm, BAS-2500). Moreover, the readout was initiated at least 30 minutes after the end of the exposure to reduce the fading effect of the IP during the readout.[37]

D. Evaluation of Dislocation Density and Its Properties

The modified Williamson–Hall plot and the modified Warren–Averbach method were employed to quantify the dislocation density of the ULC steel wires, as proposed by Ungár et al.[38] The modified Williamson–Hall plot can be expressed as follows:

$$\Delta K \cong 0.9/D + \left(\pi A b^2/2\right)^{1/2} \rho^{1/2} \left(K^2 \overline{C}\right)^{1/2} + \left(\pi A' b^2/2\right) Q^{1/2} K^2 \overline{C},$$
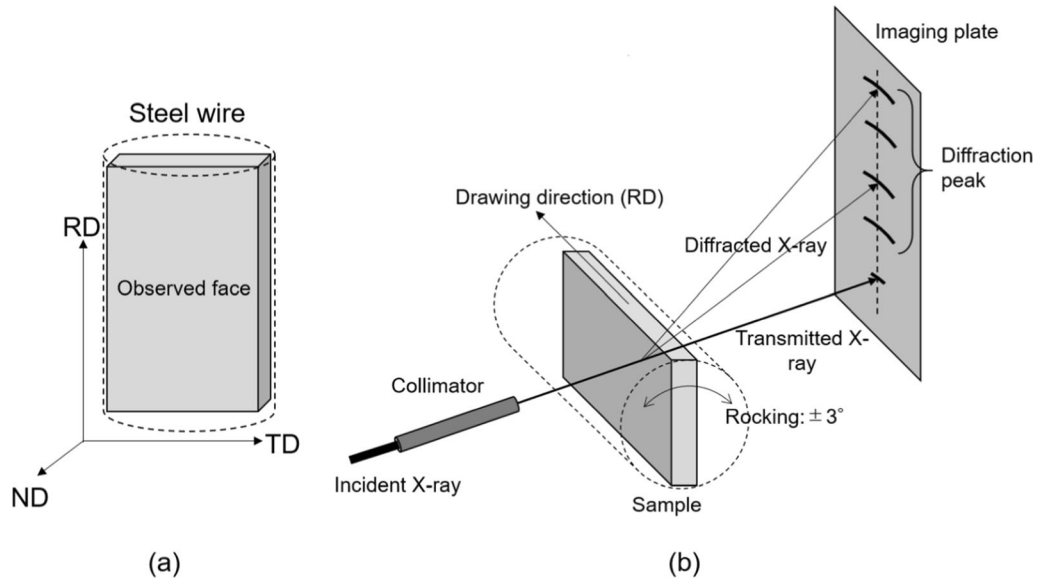
$$[1]$$

Fig. 1—Schematics of (*a*) a sample for internal structure analysis, and (*b*) the synchrotron radiation X-ray diffraction (SR-XRD) experiment.

where D is the apparent size parameter, K is defined as $2\sin(\theta)/\lambda$, ΔK is the full width at half maximum (FWHM) of an XRD profile, A and A' are parameters determined by the effective outer cut-off radius of dislocations, b is the Burgers vector, ρ is the dislocation density, and Q is the correlation factor related to the two-particle correlations in the dislocation ensemble. The average contrast factor of dislocations, $\overline{C}$, is expressed as a function of the polynomial of hkl as follows:

$$\overline{C} = \overline{C}_{h00}\left(1 - qH^2\right), \qquad [2]$$

where $\overline{C}_{h00}$ is the average dislocation contrast factor for the $h00$ reflection, which is calculated as a function of the elastic constants c_{11}, c_{22}, and c_{44},[39] H^2 is defined as $\left(h^2k^2 + h^2l^2 + k^2l^2\right)/\left(h^2 + k^2 + l^2\right)^2$, and q is a parameter that depends on the elastic constants and on the type of dislocations in the crystal (*e.g.*, edge or screw type).

In this study, the third term on the right-hand side of Eq. [1] was regarded as high-order term to obtain the average contrast factor of dislocations practically. Therefore, Eq. [1] was modified as follows:

$$\Delta K \cong 0.9/D + \left(\pi Ab^2/2\right)^{1/2}\rho^{1/2}\left(K^2\overline{C}\right)^{1/2} + O\left(K^2\overline{C}\right). \quad [3]$$

In its quadratic form it is

$$(\Delta K)^2 \cong (0.9/D)^2 + \left(\pi Ab^2/2\right)\rho K^2\overline{C} + O\left(K^4\overline{C}^2\right), \quad [4]$$

where O indicates non-interpreted higher-order terms.[39] The following equation was derived from Eqs. [2] and [4] to determine q:

$$\frac{(\Delta K)^2 - \alpha^2}{K^2} \cong \beta\overline{C}_{h00}\left(1 - qH^2\right), \qquad [5]$$

where $\alpha = 0.9/D$ and $\beta = \left(\pi Ab^2/2\right)\rho$. q was determined using a linear regression model of the left-hand side of Eq. [5] *vs* H^2.

Because $\overline{C}_{h00}$ and q depend on fraction of screw and edge dislocation components, they can be expressed with the fraction of screw dislocations, S $(0 \leqq S \leqq 1)$, as follows:

$$\overline{C}_{h00} = \overline{C}_{h00}^{\text{screw}}S + (1 - S)\overline{C}_{h00}^{\text{edge}}, \qquad [6]$$

$$q = q^{\text{screw}}S + (1 - S)q^{\text{edge}}. \qquad [7]$$

where $\overline{C}_{h00}^{\text{screw}}$ and q^{screw} correspond to pure screw dislocations, and $\overline{C}_{h00}^{\text{edge}}$ and q^{edge} correspond to pure edge dislocations. $\overline{C}_{h00}^{\text{screw}}$, $\overline{C}_{h00}^{\text{edge}}$, q^{screw}, and q^{edge} values of 0.298, 0.262, 2.652, and 1.372, respectively, were used to evaluate S and $\overline{C}_{h00}$.[40]

The modified Warren–Averbach equation for the real components of the Fourier coefficients, $A(L)$, can be expressed as follows[38,41–43]:

$$\ln A(L) \cong \ln A^{\text{S}}(L) - \rho BL^2 \ln\left(\frac{R_{\text{e}}}{L}\right)K^2\overline{C} + O\left(K^2\overline{C}\right)^2, \qquad [8]$$

where $A^{\text{S}}(L)$ are the Fourier coefficients of the size profiles, ρ is the dislocation density, B is defined as $\pi b^2/2$ (*b*: the Burgers vector of dislocations), L is the Fourier variable, R_{e} is the effective outer cut-off radius of the dislocations, and O represents higher-order terms in $K^2\overline{C}$.[38] Therefore, all the peaks were fitted using Voigt functions, and the properties of these functions were used to determine the Fourier coefficients. ρ and R_{e} were evaluated using the equation, $Y(L) = \rho BL^2 \ln(R_{\text{e}}/L)$, which represented the coefficient of the first-order term of $K^2\overline{C}$ in Eq. [8] for each value of L. The effective outer
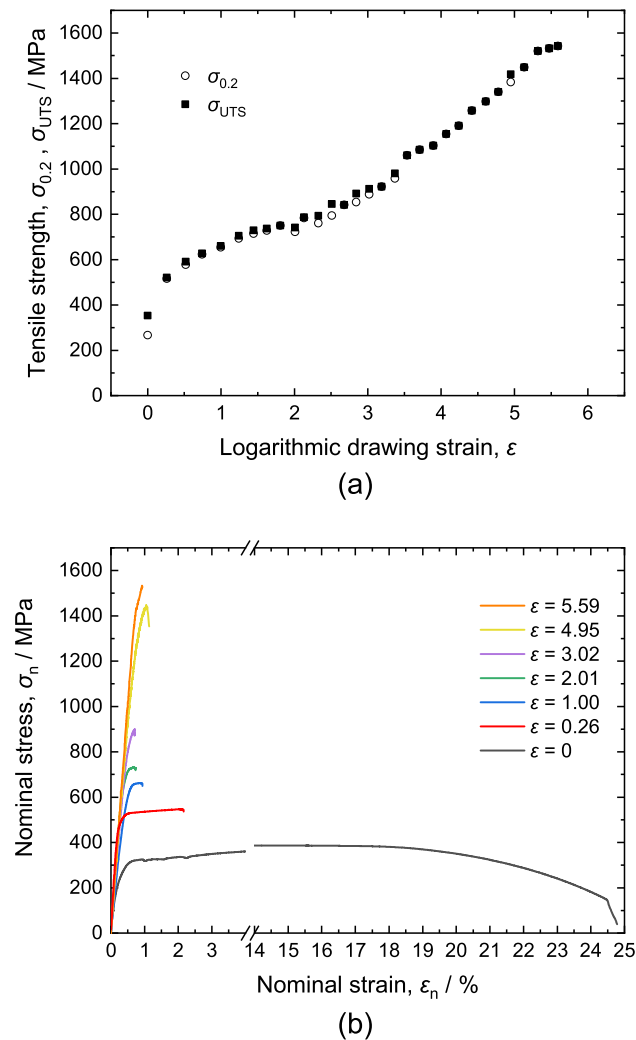
Fig. 2—Mechanical properties of drawn ULC steel wires. (a) 0.2 pct proof stress ($\sigma_{0.2}$, ○) and ultimate tensile strength (σ_{UTS}, ■) as functions of logarithmic drawing strain. (b) Representative nominal stress–strain curves of the drawn ULC steel wires (Color figure online).

cut-off radius of dislocation, R_e^*, reported by Wilkens[44] was calculated as follows: $R_e^* = R_e / \exp(2)$.[45]

III. RESULTS

A. Mechanical Properties and Internal Structure Evolution of Cold-Drawn ULC Steel Wires

Figure 2(a) shows the 0.2 pct proof stress ($\sigma_{0.2}$) and the ultimate tensile strength (σ_{UTS}) of the drawn ULC steel wires as a function of the logarithmic drawing strain (ε). Representative nominal stress–strain curves of the drawn ULC steel wires are shown in Figure 2(b). The elastic modulus of the initial steel wire ($\varepsilon = 0$) and the drawn steel wires other than the wire after the first drawing ($\varepsilon = 0.26$) ranged from 200 to 210 GPa. The elastic modulus of the drawn steel wire after the first drawing was 250 GPa, which may be attributed to reducing preferred orientation compared to other wires,

as shown in Figure 5. The $\sigma_{0.2}$ and σ_{UTS} of the initial steel wire were estimated to be 267 and 353 MPa, respectively. The post-drawing $\sigma_{0.2}$ was almost identical to σ_{UTS}; moreover, $\sigma_{0.2}$ and σ_{UTS} increased to 520 MPa after the first drawing, which was 1.5 to 2 times the initial value. The increase in $\sigma_{0.2}$ and σ_{UTS} gradually diminished after the second drawing ($\varepsilon = 0.52$) with increasing logarithmic drawing strain, and saturated at approximately 750 MPa from the sixth drawing ($\varepsilon = 1.44$) to the ninth drawing ($\varepsilon = 2.01$). $\sigma_{0.2}$ and σ_{UTS} increased again after the tenth drawing ($\varepsilon = 2.13$) in an almost proportional manner to the logarithmic drawing strain. The maximum value of σ_{UTS} (1543 MPa at $\varepsilon = 5.59$) was more than four times greater than the σ_{UTS} of the initial steel wire.

Figure 3 shows the ECC images of the drawn ULC steel wires. Since ECC imaging provides crystallographic microstructures of a sample, the technique is useful for characterizing crystalline grain shape and deformation substructure in the drawn steel wire by SEM. Figure 4 shows the EBSD maps of the drawn ULC steel wires. The inverse pole figure (IPF) color and image quality (IQ) maps were overlaid on the EBSD maps. The IPF color map provides information regarding crystalline orientation along the direction normal to the observation surface as a color map, and the IQ map indicates the quality of the EBSD patterns, reflecting the deformation of crystalline grains; moreover, the grain boundaries are represented by lines with darker contrast in the IQ maps. The initial steel wire ($\varepsilon = 0$) had isotropic crystalline grains (Figures 3(a) and 4(a)), which deformed and elongated along the wire drawing direction with increasing logarithmic drawing strain, as shown in Figures 3(b) through (f) and 4(b) through (h), and tended to show lamellar grains. Moreover, the sub-grain boundaries were generated in the deformed crystalline grains. Figure 5 shows orientation distribution function (ODF) maps along the wire drawing direction of the drawn ULC steel wire obtained using the EBSD results. The crystalline grains in the initial steel wire already had a strong preferred orientation of $\langle 110 \rangle$ along the wire drawing direction. The first drawing reduced the preferred orientation, but as the number of drawings and the logarithmic drawing strain increased, the crystalline grains in the drawn steel wires elongated along the wire drawing direction, and the preferred orientation of $\langle 110 \rangle$ became stronger again.

The variations in the nature of the grain boundaries, including the sub-grain boundaries, with drawing were investigated by classifying them into three types: high-angle boundaries (HABs) with misorientation angles of 15 deg or more, low-angle boundaries with misorientation angles of 5 deg or more but less than 15 deg (LABs-1), and low-angle boundaries with misorientation angles of 2 deg or more but less than 5 deg (LABs-2). Since the angular accuracy of the data obtained from EBSD measurements ranges from 0.5 to 1 deg, low-angle grain boundaries with misorientation angles less than 2 are were excluded from LABs-2. Figure 6 shows the grain boundary maps obtained using the EBSD measurement data corresponding to logarithmic drawing strains greater than 2.51. The HABs, LABs-1, and LABs-2 are indicated on the maps by the blue, green, and
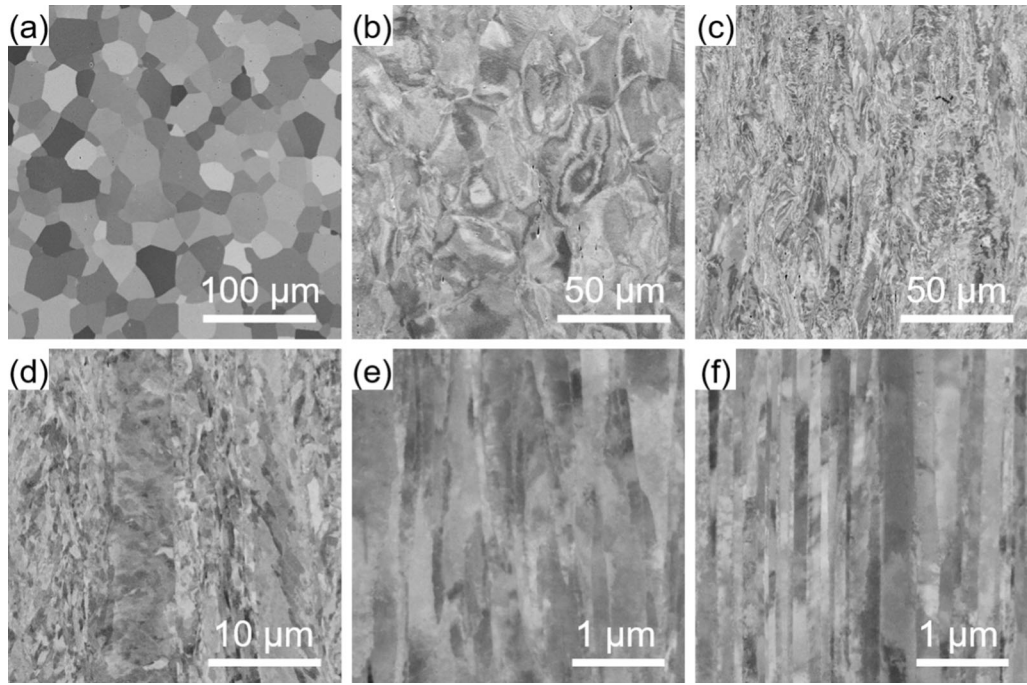
Fig. 3—Electron channeling contrast images showing internal structure of drawn ULC steel wires at logarithmic drawing strains of (*a*) 0, (*b*) 0.26, (*c*) 1.00, (*d*) 2.01, (*e*) 4.07, and (*f*) 5.59.
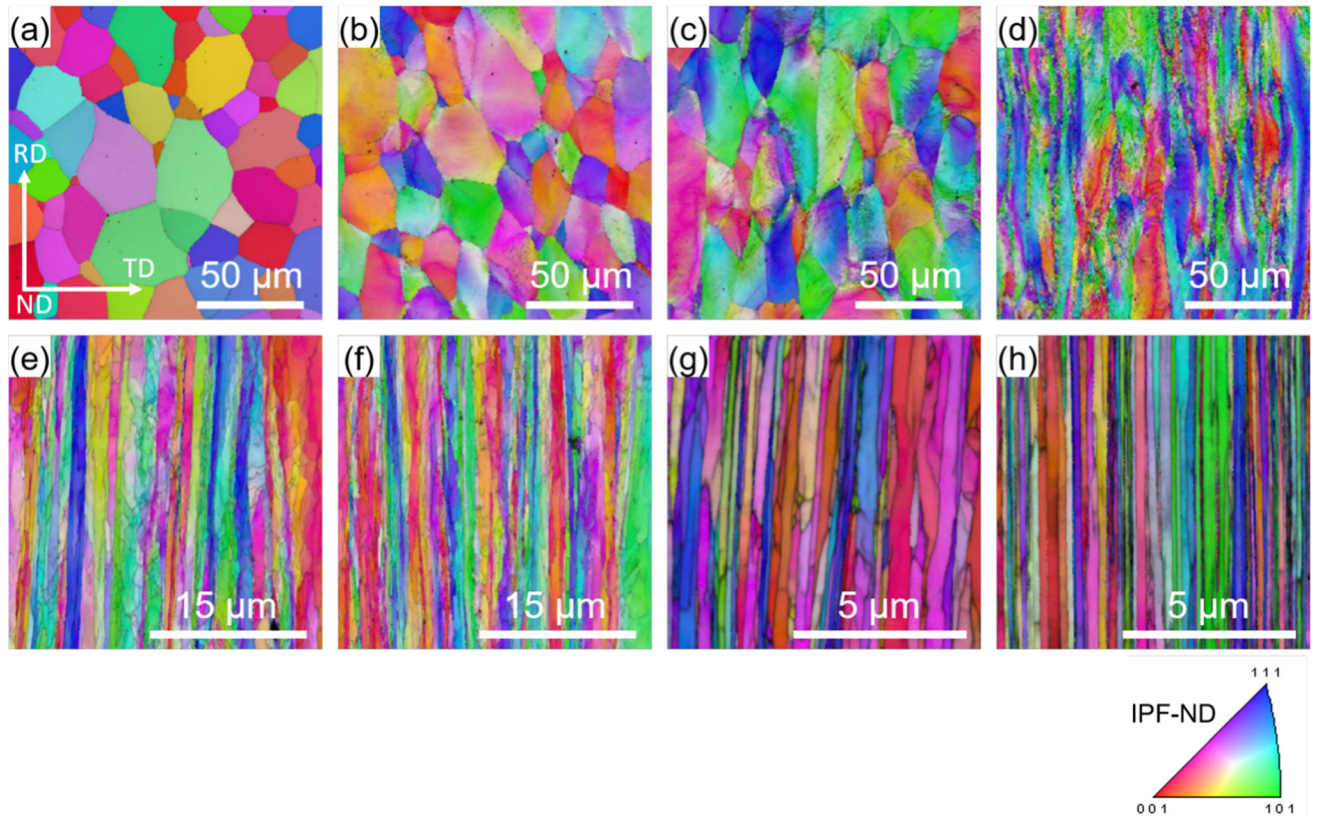

Fig. 4—EBSD maps of drawn ULC steel wires at logarithmic drawing strains of (*a*) 0, (*b*) 0.26, (*c*) 0.52, (*d*) 1.44, (*e*) 2.51, (*f*) 3.02, (*g*) 3.54, and (*h*) 5.59. Inverse pole figure (IPF) color and image quality (IQ) maps have been overlaid. RD and ND represent the wire drawing direction and the direction normal to the observation surface, respectively. The IPF maps provide information regarding crystalline orientation along ND. The step size and scan area for EBSD mapping are set to 0.5 μm and 300 μm $\times$ 300 μm for (a) through (d), 0.1 μm and 40 μm $\times$ 40 μm for (e) and (f), and for 0.04 μm and 15 μm $\times$ 15 μm for (g) and (h), respectively (Color figure online).
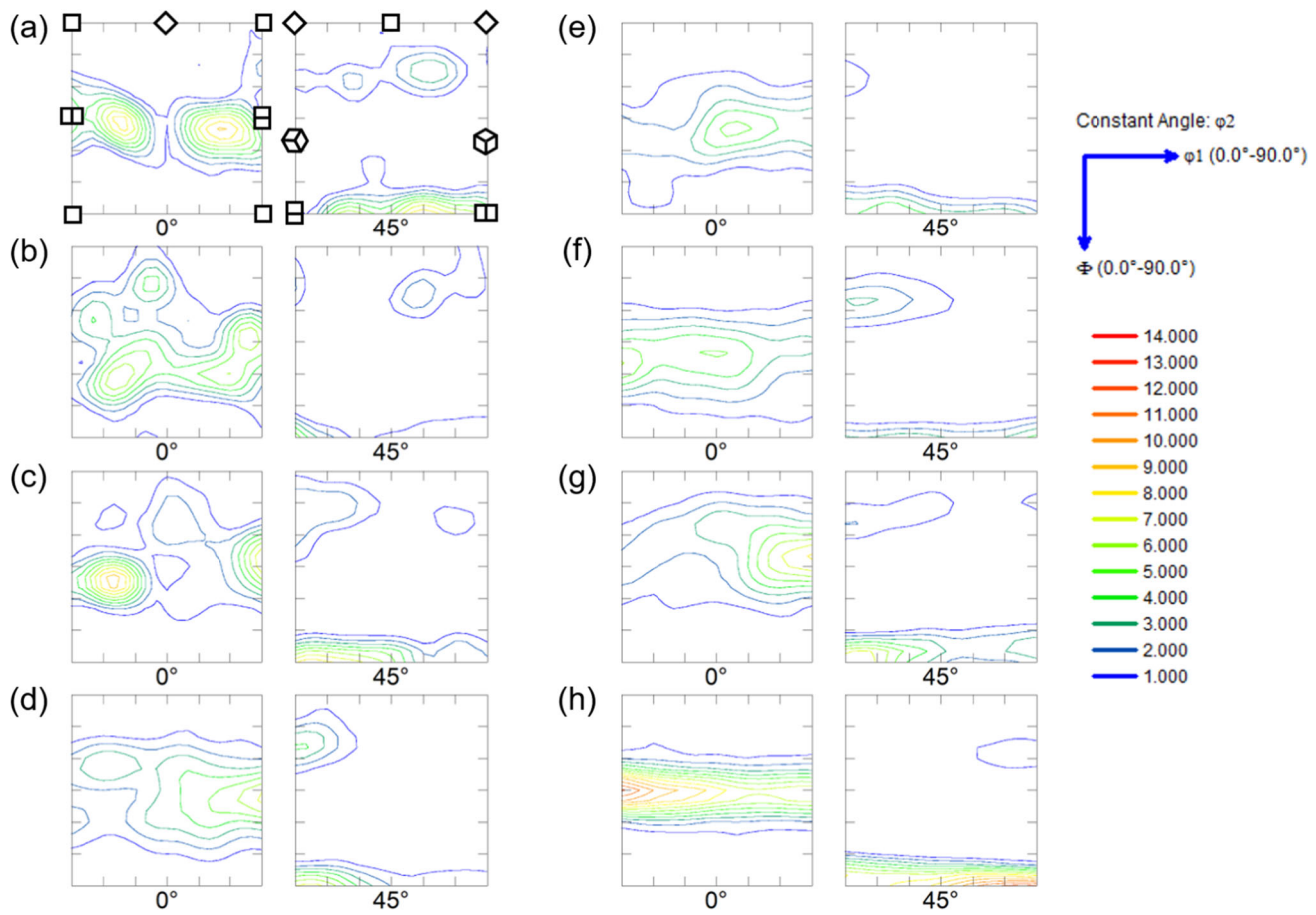
Fig. 5—Orientation distribution function (ODF) maps acquired along RD at logarithmic drawing strains of (*a*) 0, (*b*) 0.26, (*c*) 0.52, (*d*) 1.44, (*e*) 2.51, (*f*) 3.02, (*g*) 3.54, and (*h*) 5.59 (Color figure online).
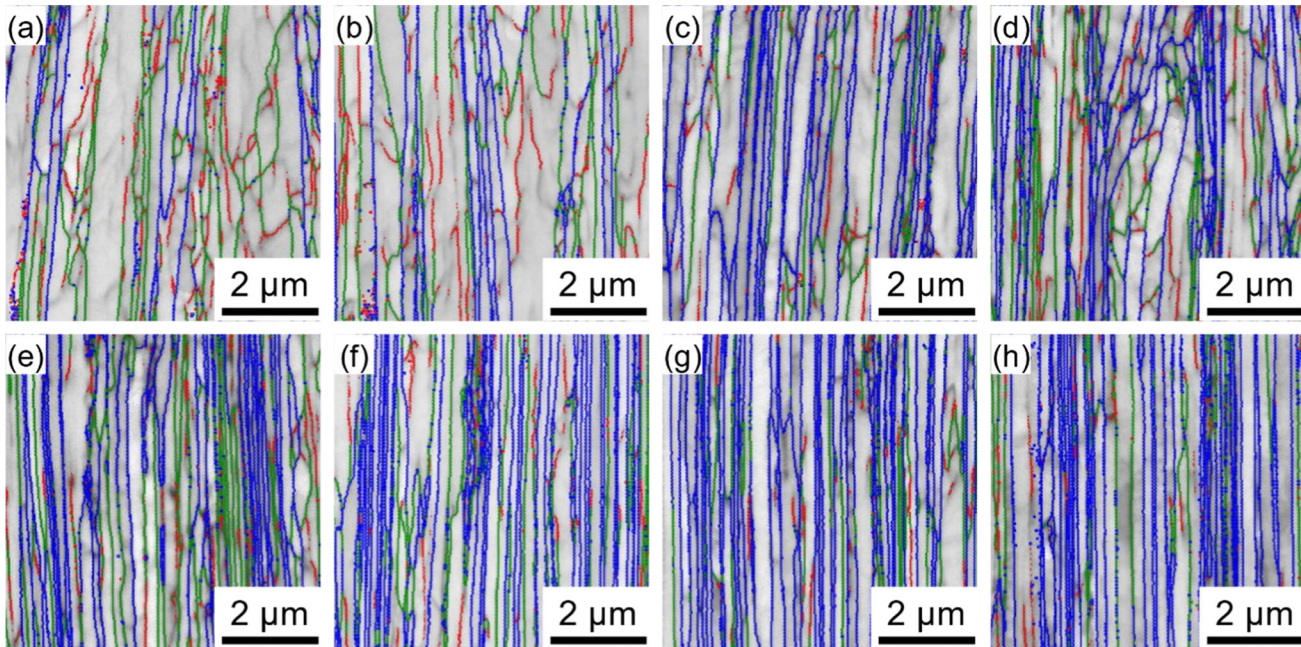

Fig. 6—HABs, LABs-1, and LABs-2 (blue, green, and red solid lines, respectively) in the drawn ULC steel wires corresponding to logarithmic drawing strains of (*a*) 2.51, (*b*) 3.02, (*c*) 3.54, (*d*) 4.07, (*e*) 4.61, (*f*) 5.13, (*g*) 5.32, and (*h*) 5.59 (Color figure online).
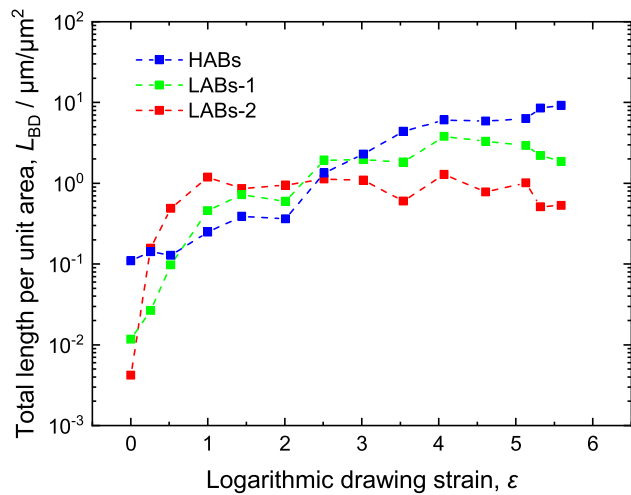
Fig. 7—Variations in total length per unit area of the HABs (blue), LABs-1 (green), and LABs-2 (red) of the drawn ULC steel wires as a function of logarithmic drawing strain (Color figure online).

Fig. 8—Averaged crystalline grain width (d_{grain}) as a function of wire diameter (d_{wire}).

Fig. 9—Variations in the widths (FWHM; ΔK) of the diffraction peaks as a function of logarithmic drawing strain (Color figure online).

red solid lines, respectively. The grain boundaries consisted mainly of HABs and LABs-1, while LABs-2 existed within the grains as sub-grain boundaries. The total lengths of the grain boundary per unit area (L_{BD}) are shown in Figure 7. The L_{BD} of HABs (0.1 $\mu m/\mu m^2$ in the initial steel wire) monotonically increased after the first drawing (ε = 0.26), reached 1×10^{-1} $\mu m/\mu m^2$ at ε = 2.01. After ε = 2.01, the L_{BD} of HABs increased at a larger incremental rate, and reached 10 $\mu m/\mu m^2$ at ε = 5.56. The L_{BD} of LABs-1 (1×10^{-2} $\mu m/\mu m^2$ in the initial steel wire) quickly increased after the first drawing, reached 5×10^{-1} $\mu m/\mu m^2$ at ε = 1.00, thereafter gradually increased with increasing logarithmic drawing strain, reached 4 $\mu m/\mu m^2$ at ε = 1.00, and then decreased to 3 $\mu m/\mu m^2$. The L_{BD} of LABs-2 (4×10^{-3} $\mu m/\mu m^2$ in the initial steel wire) quickly increased after the first drawing, reached 1 $\mu m/\mu m^2$ at ε = 1.00, and saturated thereafter around 1 $\mu m/\mu m^2$ with increasing logarithmic drawing strain.

Figure 8 shows the averaged crystalline grain width (d_{grain}) of the drawn wires as a function of their diameters (d_{wire}). Because the crystalline grains of the drawn wires were found to be elongated along the wire drawing direction (Figures 3, 4, and 6), the averaged spacing of HABs was measured along the direction perpendicular to the wire drawing direction, and the space was regarded as d_{grain}. The d_{grain} parameter gradually and drastically decreased with decreasing wire diameters from 2.503 (ε = 0.52) to 1.557 mm (ε = 1.44), and from 1.577 (ε = 1.44) to 0.554 mm (ε = 3.54), respectively. The decrease in d_{grain} with decreasing wire diameters from 0.554 (ε = 3.54) to 0.198 mm (ε = 5.59) was proportional to the square root of the wire diameter.

B. Dislocation Density and Parameters for Evaluating the Dislocation Properties of Drawn ULC Steel Wires

The dislocation density and the parameters for estimating the dislocation properties were obtained by analyzing the XRD profiles by constructing the modified Williamson–Hall plot and using the modi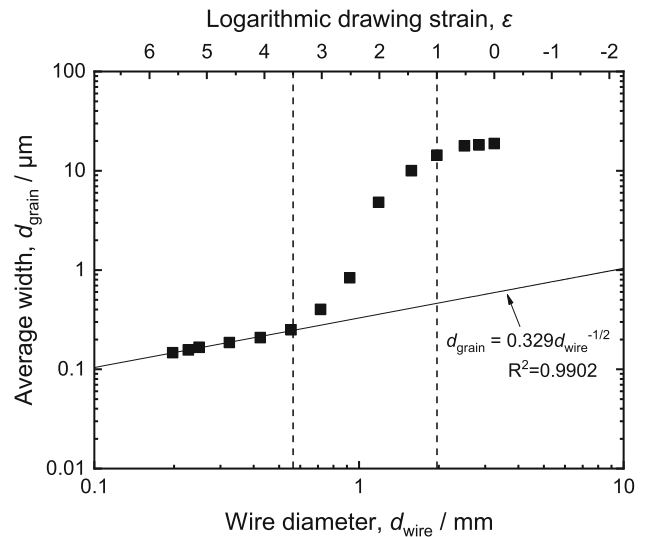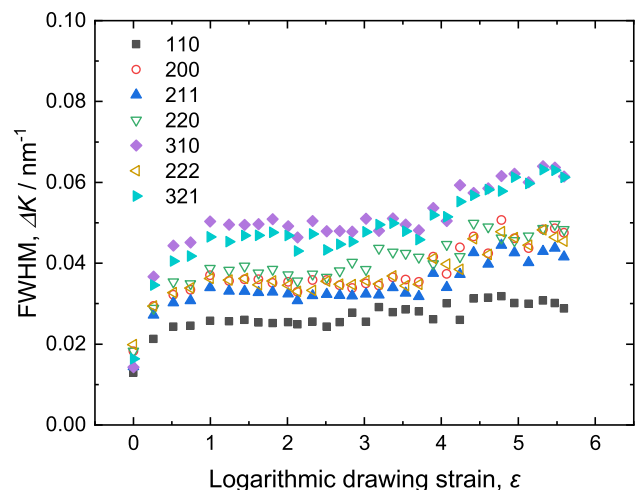fied Warren–Averbach method. Figure 9 illustrates the variations in the FWHM (ΔK) of all the XRD peaks as a function of the logarithmic drawing strain. ΔK monotonically increased with increasing logarithmic drawing strain up to the fourth drawing (ε = 1.00), saturated between ε = 1.24 and ε = 2.01, and increased with increasing logarithmic drawing strain after ε = 2.13.

Figure 10 shows the variation in crystallite size as a function of the logarithmic drawing strain. The solid and open squares represent the crystallite sizes estimated using the modified Williamson–Hall plot and modified Warren–Averbach method, respectively. The modified Williamson–Hall plot yielded a crystallite size of approximately 70 nm for the initial wire, which gradually increased to 90 nm from the first drawing (ε = 0.26) up to ε = 2.0, and remained in the 50 to 90 nm range after ε = 2.0. However, the modified Warren–Averbach method yielded a crystallite size of
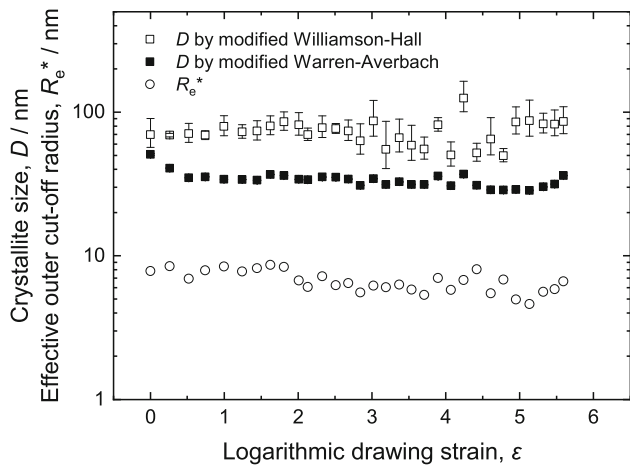
Fig. 10—Variation in crystallite size estimated using the modified Williamson–Hall plot (■) and the modified Warren–Averbach method (□), and effective outer cut-off radius (○) of dislocations for the drawn ULC steel wires as a function of the logarithmic drawing strain.
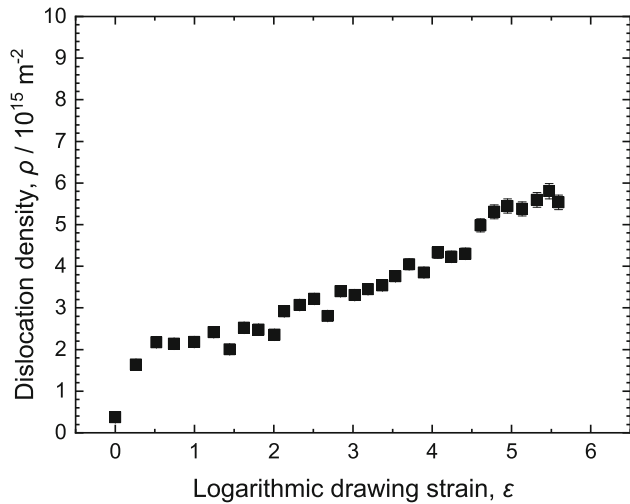

Fig. 11—Variations in dislocation density (ρ) of the drawn ULC steel wires as a function of the logarithmic drawing strain.

Fig. 12—Variations in dislocation arrangement parameter (M^*), and the q parameter of the drawn ULC steel wires as functions of the logarithmic drawing strain.

approximately 50 nm for the initial wire, which gradually decreased to 30 nm with increasing logarithmic drawing strain. It may effect on the dislocation density in the crystal, the change in crystallite size due to the drawing process is, however, so small that its effect on the change in dislocation density is also expected to be small. Therefore, its contribution to the strength of the wires is considered to be small. Figure 10 also shows the effective outer cut-off radius (R_e^*) of dislocations estimated using the modified Warren–Averbach method as a function of the logarithmic drawing strain. R_e^* was estimated to be in the 5 to 10 nm range, and gradually decreased with increasing logarithmic drawing strain.

Figure 11 shows the dislocation density (ρ) estimated using the modified Warren–Averbach method as a function of the logarithmic drawing strain. The dislocation density increased with increasing logarithmic
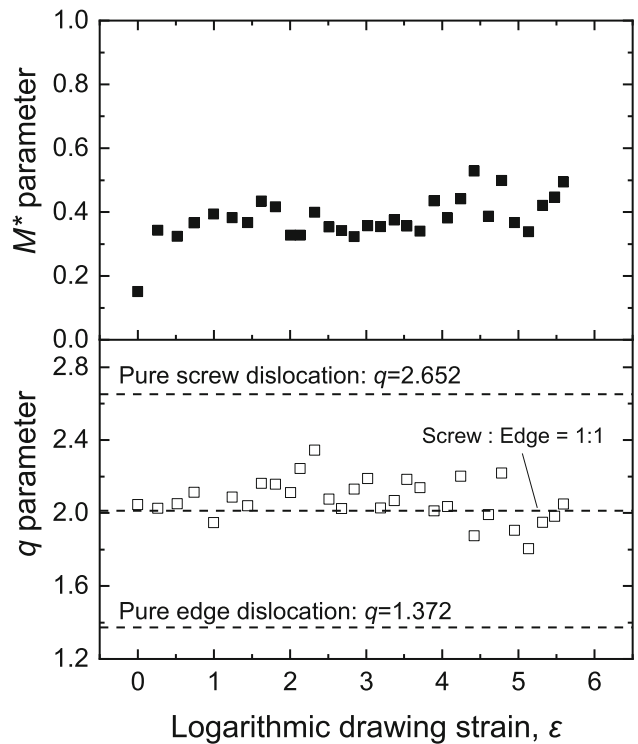
drawing strain up to the second drawing ($\varepsilon = 0.52$), where the density was 5 times greater than that of the initial wire. Moreover, ρ appeared to saturate from the third drawing ($\varepsilon = 0.74$) to the ninth drawing ($\varepsilon = 2.01$), and increased with increasing logarithmic drawing strain thereafter. The dislocation arrangement parameter (M^*), which indicates the interactive effect between dislocations, is expressed as $M^* = R_e^*\sqrt{\rho}$; the dislocations are randomly distributed for M^* value greater than 1, and have cellular structures or dipole characteristic for M^* value < 1[44,46]. Figure 12 shows that M^* is smaller than 0.2 in the initial steel wire, revealing the cellular structures or dipole characteristic of the dislocations, and that the dislocations still have the cellular structures or dipole characteristic after drawing. Figure 12 also shows the variation in q obtained using the drawn ULC steel wires as a function of the logarithmic drawing strain. The q parameter varied in the 1.80 to 2.35 range, and no systematic changes in q were observed with the logarithmic drawing strain of the drawn wires. These results indicate that the wire drawing did not cause obvious and systematic changes in the dislocation properties of the drawn ULC steel wire. Additionally, the trend of variation of the M^* and q parameters is similar as a function of logarithmic drawing strain, except at strain near ~ 2.0 although these two parameters vary in a narrow range. The M^* parameter depends on the effective outer cut-off radius of dislocation (R_e^*), which indicates strain field distribution around dislocations. The q parameter indicates the fraction of screw and edge dislocation components.

Therefore, the trend of variation of these two parameters may suggest that the strain field distribution around the dislocations of the drawn ULC steel wire depends on the fraction of screw and edge components.

IV. DISCUSSION

The effects of dislocation density and grain size on the strengthening behavior of the drawn ULC steel wires were examined to comprehensively elucidate the strengthening behavior. In this regard, the contributions of the effects of dislocations (σ_{dis}) and grain size (σ_{g-s}) to the strengthening behavior were assumed to be additive, and the effect of precipitation was assumed to be negligible because of the small number of precipitates, such as carbides and nitrides, in the ULC steel wires. σ_{dis} was considered to increase according to the Bailey–Hirsch relationship,[47] and σ_{g-s} was presumed to
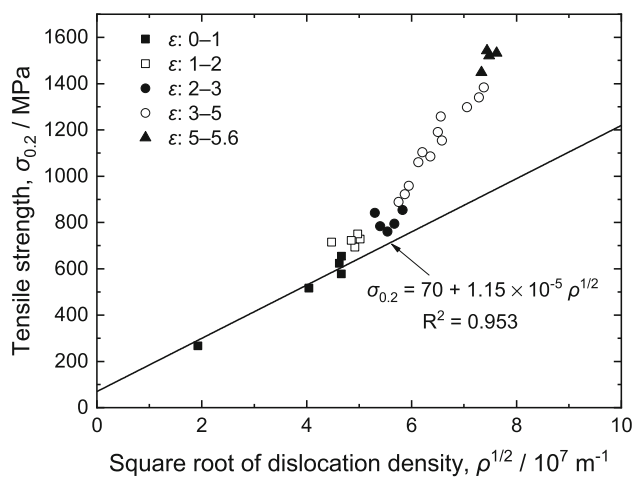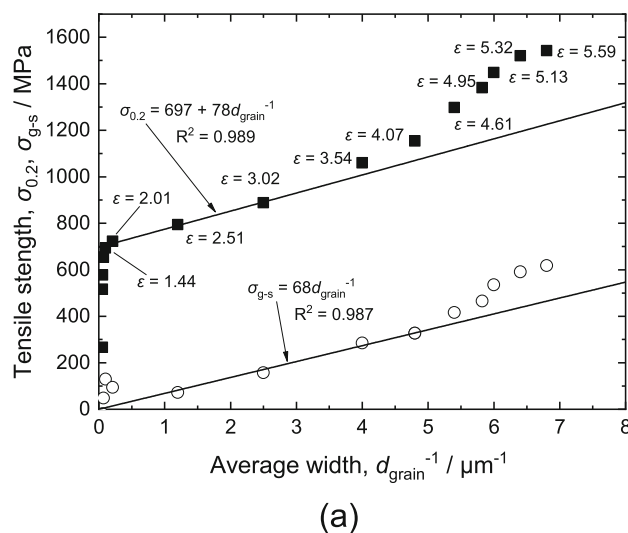
increase according to the Langford–Cohen or Hall–Petch relationship. Therefore, the flow stress (σ) of the drawn ULC steel wires could be expressed as follows:

$$\sigma = \sigma_{dis} + \sigma_{g-s} = \sigma_0 + \alpha G b\sqrt{\rho} + k_{L-C}/d_{grain}$$
$$\text{(for the Langford–Cohen relationship),} \quad [9]$$

or

$$\sigma = \sigma_{dis} + \sigma_{g-s} = \sigma_0 + \alpha G b\sqrt{\rho} + k_{H-P}/\sqrt{d_{grain}}$$
$$\text{(for the Hall–Petch relationship),} \quad [10]$$

where σ_0 is the yield strength, α is a constant, G is the shear modulus (= 80 GPa for iron), b is the Burgers vector (0.248 nm), ρ is the dislocation density, and k_{L-C} and k_{H-P} are coefficients for the Langford–Cohen and Hall–Petch relationships, respectively. 0.2 pct proof stress, $\sigma_{0.2}$, was used as the flow stress in Eqs. [9] and [10] in this analysis.

Figure 13 shows the $\sigma_{0.2}$ of the drawn ULC steel wires as a function of the square root of the dislocation density. Figures 14(a) and (b) show the variations in $\sigma_{0.2}$ as functions of the inverse of d_{grain} and the inverse of the square root of d_{grain}, respectively. The $\sigma_{0.2}$ increased in proportion to the square root of the dislocation density from $\varepsilon = 0$ to $\varepsilon = 1$, as shown in Figure 13; however, the change in d_{grain} was small in this logarithmic drawing strain range, and the evaluation of the dependence of $\sigma_{0.2}$ on d_{grain} was difficult (Figure 14). This suggests that the effects of dislocation were more dominant than those of grain size in the ε range of 0 to 1. Therefore, the terms representing the grain size effects in Eqs. [9] and [10] were neglected, and the resulting fits of the $\sigma_{0.2}$ data from $\varepsilon = 0$ to $\varepsilon = 1$ yielded $\sigma_0 = 70$ MPa and $\alpha G b = 1.15 \times 10^{-5}$ MPa m. These values are consistent with those of previously reported pure iron and IF ferrite steel.[48,49] The increase in $\sigma_{0.2}$ deviated from the Bailey–Hirsch relationship after $\varepsilon = 1$, as shown in Figure 13, and followed the
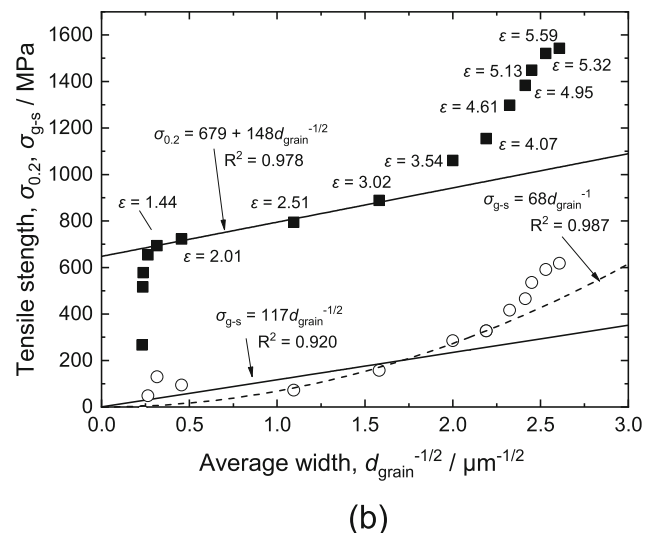

Fig. 13—Variation in tensile strength ($\sigma_{0.2}$) as a function of the square root of dislocation density.

(a)

(b)

Fig. 14—Variations in $\sigma_{0.2}$ (■) and σ_{g-s} (○) as a function of (a) the inverse of average grain width and (b) the inverse of the square root of average grain width.

Langford–Cohen relationship or the Hall–Petch relationship, as shown in Figure 14. This suggests that the effects of grain size became more dominant than those of dislocations after $\varepsilon = 1$. In addition, the $\sigma_{0.2}$ values corresponding to $\varepsilon > 3.5$ deviated from the extrapolation calculated following the Langford–Cohen relationship or the Hall–Petch relationship using the data in the ε range of 1.44 to 3.02.

Figures 14(a) and (b) also show the variations in σ_{g-s} as functions of the inverse of d_{grain} and the inverse of the square root of d_{grain}, respectively. The σ_{g-s} values were obtained with subtracting σ_{dis} from $\sigma_{0.2}$. The σ_{dis} values were calculated based on the Bailey–Hirsch relationship using the parameters of $\sigma_0 = 70$ MPa and $\alpha Gb = 1.15 \times 10^{-5}$ MPa m. As shown in Figure 14, the σ_{g-s} increased according to the Langford–Cohen relationship rather than the Hall–Petch relationship. The Langford–Cohen coefficient (k_{L-C}) in the ε range of 1.00–4.07 was estimated to be 6.8×10^{-5} MPa m. The σ_{g-s} values corresponding to $\varepsilon > 4.07$ showed a positive deviation from the extrapolation calculated following the Langford–Cohen relationship using k_{L-C} in the ε range of 1.00 to 4.07. Therefore, excessive strengthening similar to the extra Hall–Petch strengthening[36] was confirmed to occur in the drawn ULC steel wires.

In the past, two separate Hall–Petch relationships have been used to determine the contribution of LABs and HABs to flow stress.[36,50,51] However, as shown in Figure 7, the total length per unit area of LABs (LABs-1 and LABs-2) is almost saturated in the region of logarithmic drawing strain, where strengthening occurs following the Langford–Cohen relationship or the Hall–Petch relationship, making it unlikely that LABs exhibit the Langford–Cohen relationship or the Hall–Petch relationship. In this section, the correlation between changes in HABs, LABs-1, and LABs-2 and changes in σ_{g-s} was considered to investigate the cause of the excessive strengthening of σ_{g-s} shown in Figure 14. The grains in the drawn steel wires elongated along the wire drawing direction with increasing logarithmic drawing strain (Figures 3 and 4) and exhibited a lamellar shape at $\varepsilon = 2.51$. The grain boundaries consisted mainly of HABs and LABs-1, as shown in Figure 6, while LABs-2 existed within the grains as sub-grain boundaries; the total length per unit area of HABs increased monotonically with increasing logarithmic drawing strain, increased to 4 times that of the initial steel wire at $\varepsilon = 1$. The total length per unit area of LABs-1 also increased monotonically with increasing logarithmic drawing strain at a greater rate of increase than that of HABs, increased 40 times that of the initial steel wire at $\varepsilon = 1$. The total length per unit area of LABs-2 increased drastically after the first drawing ($\varepsilon = 0.26$) to 300 times that of the initial steel wire, exceeded the total length per unit area of HABs and LABs-1. Up to $\varepsilon = 1$ after the first drawing, the total length per unit area of LABs-2 exceeds that of HABs and LABs-1. Since LABs-2 is most likely a dislocation source, it is possible that LABs-2 contributes to dislocation hardening at $\varepsilon = 0$ to 1.

For $\varepsilon > 1$, the length per unit area of LABs-2 hardly increases, while the length per unit area of HABs and LABs-1 monotonically increases up to $\varepsilon = 2.51$, with the total length of LABs-1 exceeding that of HABs. As mentioned earlier, the grain boundaries in the drawn ULC steel wire consist of HABs and LABs-1, which are considered to act as sinks for dislocations.[52] Their total length per unit area increases, while the total length per unit area of LABs-2, which can easily act as a dislocation source, hardly increases. This behavior of grain boundaries (HABs and LABs-1) and sub-grain boundaries (LABs-2) is thought to have a significant effect on grain boundary strengthening. Furthermore, for $\varepsilon > 3$, HABs greatly exceeded LABs-1, and this increase in the total length per unit area of HABs may be possible for the increase in the Langford–Cohen coefficient of drawn ULC steel wire at $\varepsilon > 3$.

An investigation of the strengthening mechanism of ultrafine-grained and sub-fine-grained high-purity aluminum[36] revealed that low-angle grain boundaries with misorientation angles greater than 2 deg acted as conventional grain boundaries for dislocation glide and contributed to the strength. The results discussed herein related to the contributions of HABs and LABs-1 to the strength, and the effects of the HABs and LABs-1 fractions on the Langford–Cohen coefficients are remarkably similar to previously obtained results.[36] When a relatively large number of LABs-2 are present in the grain compared to HABs and LABs-1, an increase in tensile strength due to dislocation effects would be expected. HABs and LABs-1 acting as grain boundaries may contribute to the change in tensile strength due to the grain size effect, and the increase in tensile strength is accelerated when there are more HABs than LABs-1.Therefore, the variation in the character of the grain boundaries due to wire drawing must be considered along with the changes in dislocation density and grain size to elucidate the strengthening behavior of the drawn ULC steel wires.

V. CONCLUSIONS

The microstructural evolution and variation in dislocation properties and dislocation density of ULC steel wires during drawing were investigated by SEM/EBSD and SR-XRD. The ultimate tensile strength of the drawn ULC steel wires reached a maximum value of 1543 MPa at $\varepsilon = 5.6$. The crystalline grains of the drawn ULC steel wires were elongated and tended to show lamellar grains which have the preferred orientation of $\langle 110 \rangle$ along the wire drawing direction. In the early stage of drawing ($\varepsilon = 0$ to 1), the 0.2 pct proof stress of the drawn ULC steel wire ($\sigma_{0.2}$) increased in accordance with the Bailey–Hirsch relationship, and the contribution of the effects of dislocations (σ_{dis}) was dominant. However, $\sigma_{0.2}$ increased at $\varepsilon > 1$ according to the Langford–Cohen or Hall–Petch relationship, and the contribution of the effects of grain size (σ_{g-s}) superseded that of the effects of dislocations. σ_{g-s} increased according to the Langford–Cohen relationship

rather than the Hall–Petch relationship. Furthermore, the σ_{g-s} values at $\varepsilon > \sim 4$ showed a positive deviation from the extrapolated Langford–Cohen relationship in the early stages of drawing, indicating the occurrence of excessive strengthening in the drawn ULC steel wires. The dislocation properties such as the fraction of screw and edge dislocation components and the dislocation arrangement of the drawn ULC steel wires did not show any systematic change with the degree of drawing, suggesting that the excessive strengthening was presumed to be induced by changes in the character of the grain boundaries rather than changes in dislocation properties during the process of drawing. Essentially, a relative decrease in the fraction of low-angle boundaries with misorientation angles in the 2 to 5 deg range (LABs-2) with the increase in high-angle boundaries with misorientation angles of 15 deg or greater (HABs) contributed to an increase in the Langford–Cohen coefficient. The HABs are considered to act as dislocation sinks, whereas the LABs-2 in the grain lamellae are considered to act as a dislocation source. Therefore, the effects of grain boundaries on strengthening were significantly larger at higher logarithmic drawing strains because of the considerably smaller number of mobile dislocations in the grains. In general, the texture is considered to influence the flow stress. However, the crystalline grains in the initial ULC steel wire already had a strong preferred orientation of ⟨110⟩ along the wire drawing direction. The first drawing reduced the preferred orientation, but as the number of drawings and the logarithmic drawing strain increased, the preferred orientation of ⟨110⟩ became stronger again. Therefore, the effect of texture on the flow stress was not considered to be noticeable in this study.

ACKNOWLEDGMENTS

CONFLICT OF INTEREST

On behalf of all authors, the corresponding author states that there is no conflict of interest.

REFERENCES

1. Y. Saito, H. Utsunomiya, N. Tsuji, and T. Sakai: *Acta Mater.*, 1999, vol. 47, pp. 579–83.
2. N. Tsuji, Y. Ito, Y. Saito, and Y. Minamino: *Scripta Mater.*, 2022, vol. 47, pp. 893–99.
3. R.Z. Valiev, R.K. Islamgaliev, and I.V. Alexandrov: *Prog. Mater. Sci.*, 2000, vol. 45, pp. 103–89.
4. B.Q. Han, E.J. Lavernia, and F.A. Mohamed: *Metall. Mater. Trans. A*, 2004, vol. 35A, pp. 1343–50.
5. K. Hajizadeh, V. Abbasi-Chianeh, and K.J. Kurzydlowski: *Appl. Phys. A*, 2022, vol. 128, p. 806.
6. C.C. Koch: *Nanostruct. Mater.*, 1997, vol. 9, pp. 13–22.
7. Y. Xu, Z.G. Liu, M. Umemoto, and K. Tsuchiya: *Metall. Mater. Trans. A*, 2002, vol. 33A, pp. 2195–2203.
8. Z. Hou, X. Wei, W. Zhang, Z. Yuan, H. Yong, and Q. Ge: *J. Iron Steel Res. Int.*, 2021, vol. 28, pp. 1329–40.
9. R.Z. Valiev, Y.V. Ivanisenko, E.F. Rauch, and B. Baudelet: *Acta Mater.*, 1996, vol. 44, pp. 4705–12.
10. A.P. Zhilyaev, S. Lee, G.V. Nurislamova, R.Z. Valiev, and T.G. Langdon: *Scripta Mater.*, 2001, vol. 44, pp. 2753–58.
11. S.H. Mousavi Anijdan, H.R. Koohdar, M. Nili-Ahmadabadi, H.R. Jafarian, and T.G. Langdon: *Mater. Sci. Eng. A*, 2022, vol. 851, p. 143660.
12. G. Langford, M. Cohen, and A.S.M. Trans: *Quart.*, 1969, vol. 62, pp. 623–38.
13. D. Kuhlmann-Wilsdorf: *Metall. Trans.*, 1970, vol. 1, pp. 3173–79.
14. H. Feng, F. Fang, X. Zhou, X. Zhang, Z. Xie, and J. Jiang: *Mater. Sci. Eng. A*, 2020, vol. 796, 140017.
15. H. Feng, L. Wang, S. Cui, N. Hansen, F. Fang, and X. Zhang: *Scripta Mater.*, 2021, vol. 200, p. 113906.
16. G. Langford: *Metall. Trans.*, 1970, vol. 1, pp. 465–77.
17. G. Langford: *Metall. Trans. A*, 1977, vol. 8A, pp. 861–75.
18. M. Zelin: *Acta Mater.*, 2002, vol. 50, pp. 4431–47.
19. Y. Ivanisenko, W. Lojkowski, R.Z. Valiev, and H.-J. Fecht: *Acta Mater.*, 2003, vol. 51, pp. 5555–70.
20. A. Hohenwarter, A. Taylor, R. Stock, and R. Pippan: *Metall. Mater. Trans. A*, 2011, vol. 42A, pp. 1609–18.
21. X. Zhang, A. Godfrey, N. Hansen, and X. Huang: *Acta Mater.*, 2013, vol. 61, pp. 4898–4909.
22. E.O. Hall: *Proc. Phys. Soc. B*, 1951, vol. 64, pp. 747–53.
23. N.J. Petch: *J. Iron Steel Inst.*, 1953, vol. 174, pp. 25–28.
24. X. Sauvage, J. Copreaux, F. Danoix, and D. Blavette: *Philos. Mag. A*, 2000, vol. 80, pp. 781–96.
25. K. Hono, M. Ohnuma, M. Murayama, S. Nishida, A. Yoshie, and T. Takahashi: *Scripta Mater.*, 2001, vol. 44, pp. 977–83.
26. A. Taniyama, T. Takayama, M. Arai, and T. Hamada: *Scripta Mater.*, 2004, vol. 51, pp. 53–58.
27. N. Min, W. Li, H. Li, and X. Jin: *J. Mater. Sci. Technol.*, 2010, vol. 26, pp. 776–82.
28. S. Djaziri, Y. Li, G.A. Nematollahi, B. Grabowski, S. Goto, C. Kirchlechner, A. Kostka, S. Doyle, J. Neugebauer, D. Raabe, and G. Dehm: *Adv. Mater.*, 2016, vol. 28, pp. 7753–57.
29. Y. Li, D. Raabe, M. Herbig, P.P. Choi, S. Goto, A. Kostka, H. Yarita, C. Borchers, and R. Kirchheim: *Phys. Rev. Lett.*, 2014, vol. 113, p. 106104.
30. S. Gao, M. Chen, S. Chen, N. Kamikawa, A. Shibata, and N. Tsuji: *Mater. Trans.*, 2014, vol. 55, pp. 73–77.
31. S. Gao, M. Chen, M. Joshi, A. Shibata, and N. Tsuji: *J. Mater. Sci.*, 2014, vol. 49, pp. 6536–42.
32. C.Y. Yu, P.W. Kao, and C.P. Chang: *Acta Mater.*, 2005, vol. 53, pp. 4019–28.
33. N. Kamikawa, X. Huang, N. Tsuji, and N. Hansen: *Acta Mater.*, 2009, vol. 57, pp. 4198–4208.
34. G.M. Le, A. Godfrey, and N. Hansen: *Mater. Des.*, 2013, vol. 49, pp. 360–67.
35. K.N. Zhu, A. Godfrey, N. Hansen, and X.D. Zhang: *Mater. Des.*, 2017, vol. 117, pp. 95–103.
36. N. Kamikawa, T. Hirochi, and T. Furuhara: *Metall. Mater. Trans. A*, 2019, vol. 50A, pp. 234–48.
37. A. Taniyama, D. Shindo, and T. Oikawa: *J. Electron Microsc.*, 1996, vol. 45, pp. 232–35.
38. T. Ungár and A. Borbély: *Appl. Phys. Lett.*, 1996, vol. 69, pp. 3173–75.
39. T. Ungár, I. Dragomir, Á. Révész, and A. Borbély: *J. Appl. Cryst.*, 1999, vol. 32, pp. 992–1002.
40. T. Masumura, S. Takaki, and T. Tsuchiyama: *J. Soc. Mater. Sci. Jpn.*, 2020, vol. 69, pp. 290–92. (**in Japanese**).
41. T. Ungár, J. Gubicza, G. Ribárik, and A. Borbély: *J. Appl. Cryst.*, 2001, vol. 34, pp. 298–310.
42. T. Ungár: *Mater. Sci. Eng. A*, 2001, vol. 309–310, pp. 14–22.

43. J. Gubicza and T. Ungár: *Z. Kristallogr.*, 2007, vol. 222, pp. 567–79.
44. M. Wilkens: *Phys. Status Solidi A*, 1970, vol. 2, pp. 359–70.
45. M. Wilkens: *Fundamental aspects of dislocation theory*, Spec. Publ. 317, Vol. II, National Bureau of Standards, Washington, D. C., 1970, pp. 1195–1221.
46. M. Wilkens: *J. Appl. Cryst.*, 1979, vol. 12, pp. 119–25.
47. J.E. Bailey and P.B. Hirsch: *Philos. Mag.*, 1960, vol. 5, pp. 485–97.
48. K. Nakashima, M. Suzuki, Y. Futamura, T. Tsuchiyama, and S. Takaki: *Mater. Sci. Forum*, 2006, vol. 503–504, pp. 627–32.
49. K. Takeda, N. Nakada, T. Tsuchiyama, and S. Takaki: *ISIJ Int.*, 2008, vol. 48, pp. 1122–25.
50. N. Hansen: *Mater. Sci. Eng. A*, 2005, vol. 409, pp. 39–45.
51. B.B. Wang, G.M. Xie, L.H. Wu, P. Xue, D.R. Ni, B.L. Xiao, Y.D. Liu, and Z.Y. Ma: *Mater. Sci. Eng. A*, 2021, vol. 820, p. 141504.
52. I.J. Beyerlein, M.J. Demkowicz, A. Misra, and B.P. Uberuaga: *Prog. Mater Sci.*, 2015, vol. 74, pp. 125–210.